

# A novel probability-based diagnostic imaging with weight compensation for damage localization using guided waves

**Kehai Liu<sup>1</sup>, Shuyi Ma<sup>1</sup>, Zhanjun Wu<sup>1</sup>, Yuebin Zheng<sup>1</sup>, Xiaoxi Qu<sup>1</sup>, Yishou Wang<sup>2</sup> and Wenhua Wu<sup>1</sup>**

## Abstract

To avoid direct interpretation of the complicated ultrasonic guided wave signal and the effect of dispersion, probability-based diagnostic imaging is proposed to identify damages for guided wave-based structural health monitoring. However, the probability-based diagnostic imaging algorithm usually requires a relatively large number of actuator–sensor paths to cover the monitoring area. Therefore, a weight-compensated probability-based diagnostic imaging approach is developed to improve the ability of damage localization with higher precision under the same sensor configuration. The weight-compensated probability-based diagnostic imaging algorithm compensates for the weight difference from sensing paths with the unit weight of various positions, inhibited by the path weight difference effect on diagnostic image. The validity of the approach is assessed by identifying damages at different locations with different groups of sensing paths on a stiffened composite panel. Accurate localization results have demonstrated the effectiveness of the developed probability-based diagnostic imaging approach.

## Keywords

Guided waves, damage localization, probability-based diagnostic imaging

## Introduction

Since composite structures have been widely applied into the aerospace to provide significant weight reduction and substantial performance enhancement, various structural health monitoring (SHM) techniques for composite structures have been attracting much attention.<sup>1–6</sup> Ultrasonic guided waves are acknowledged as among the most promising tools for damage localization due to their excellent propagation capability, through-the-thickness interrogation, and high sensitivity to the changes in material or structural properties.<sup>7–11</sup> Accurate interpretation of captured guided wave signals is critical for the ultrasonic guided wave-based damage localization algorithms, while the captured signals are usually complex due to the multiple wave modes, wave dispersion, boundary reflection, noise, and so on. Therefore, some algorithms for diagnostic imaging have been developed during recent years.<sup>10,12–18</sup> Most of the aforementioned algorithms require some signal features, such as the time of flight (ToF), the propagation mode, and the corresponding group velocity.

However, as the propagation mechanism of guided wave is quite complicated in aircraft structures due to geometric and structural complexity, it is quite difficult to extract these features accurately.

To avoid direct interpretation of the ultrasonic guided wave signal and the effect of dispersion, the probability-based diagnostic imaging (PDI) has been studied intensively by many researchers. In the PDI method, the correlation analysis-based signal features in elliptical patterns for various pitch–catch sensing paths are summed to yield an easily interpretable image concerning the probability of the presence of damage in the monitoring area. Zhao et al.<sup>19</sup> introduced the PDI algorithm for active health monitoring of an aircraft wing.

<sup>1</sup>State Key Laboratory of Structural Analysis for Industrial Equipment, Dalian University of Technology, Dalian, China

<sup>2</sup>School of Aerospace Engineering, Xiamen University, Xiamen, China

## Corresponding author:

Zhanjun Wu, State Key Laboratory of Structural Analysis for Industrial Equipment, Dalian University of Technology, Dalian 116024, China.  
Email: [wuzhj@dlut.edu.cn](mailto:wuzhj@dlut.edu.cn)

The algorithm showed good performance in estimating the locations of cracks or corrosion and monitoring their growth. Koduru and Rose<sup>20</sup> improved the PDI algorithm with designed annular array sensors for mode controlling, and it showed a remarkable improvement in the ability to distinguish a real corrosion defect from any other water traces on the structure.

Nevertheless, despite its ability of delivering good performance in damage localization, the PDI algorithm usually requires a relatively large number of sensing paths to reduce the negligence of the blind zones in the monitoring area.<sup>19,21</sup> Wang et al.<sup>22</sup> found that the identification confidence was improved when more damage-impaired sensing paths were involved in the data fusion. Therefore, they proposed a concept of virtual sensing paths (VSPs) to increase the number of sensing paths in data fusion. Wu et al.<sup>23</sup> developed a methodology to optimize network for the PDI algorithm, while the points with high unit weight distribution density value have been found to dominantly cause the extremely high probability for the presence of pseudo-damages. Therefore, a relatively large number of sensing paths are required to reduce the locality of the high-value dominance, which limits the application of the PDI algorithm in damage localization to a great extent.

In this study, a weight-compensated probability-based diagnostic imaging (WCPDI) approach is developed to improve the ability of damage localization with higher precision under the same sensor configuration. Through the WCPDI algorithm, damage localization can be realized with little influence by the dominance effect of the weight distribution, which means the localization accuracy will be improved compared to the localization result merely based on the peak point of the PDI probability image. The validity of the approach is assessed by identifying the damage locations on a stiffened composite panel.

## Damage diagnostic imaging algorithm

### PDI approach

In the PDI method, an intuitive image concerning the probability of the presence of damage is formed with summing the correlation analysis-based signal features in elliptical patterns for various pitch–catch transducer pairs. Assuming that there are total  $N$  sensing paths in a sensor network, the probability of damage occurring at certain grid  $(x, y)$  can be calculated as<sup>24</sup>

$$P(x, y) = \sum_{i=1}^N DI_i \cdot W_i[R_i(x, y)] \quad (1)$$

Here,  $DI_i$  is the correlation analysis-based damage index of the  $i$ th sensing path,<sup>19</sup> which can be represented by

$$\begin{aligned} DI_i &= 1 - \rho_{u_i, v_i} = 1 - \frac{\sum_{k=1}^n (u_{ik} - \bar{u}_i)(v_{ik} - \bar{v}_i)}{\sqrt{\sum_{k=1}^n (u_{ik} - \bar{u}_i)^2 \cdot \sum_{k=1}^n (v_{ik} - \bar{v}_i)^2}} \\ &= 1 - \frac{n \sum_{k=1}^n u_{ik} v_{ik} - \sum_{k=1}^n u_{ik} \cdot \sum_{k=1}^n v_{ik}}{\sqrt{\left[ n \sum_{k=1}^n u_{ik}^2 - \left( \sum_{k=1}^n u_{ik} \right)^2 \right] \left[ n \sum_{k=1}^n v_{ik}^2 - \left( \sum_{k=1}^n v_{ik} \right)^2 \right]}} \end{aligned} \quad (2)$$

Here,  $\rho_{u_i, v_i}$  is the correlation coefficient of two discrete signals of the  $i$ th sensing path,  $u_i = \{u_{i1}, u_{i2}, \dots, u_{in}\}$  and  $v_i = \{v_{i1}, v_{i2}, \dots, v_{in}\}$ , and  $\bar{u}_i$  is the mean of  $u_i$ . And  $W_i[R_i(x, y)]$  is the weight distribution function of the  $i$ th sensing path. This weight is expected to increase with a decrease in the relative distance as a defect would cause the most significant signal change in the direct wave path, and that the signal change effect would decrease if the defect is away from the direct path of the sensor pair.<sup>19,25</sup> Wang et al.<sup>22</sup> defined the main sensing paths that are affected by damage as damage-impaired paths.  $R_i(x, y)$  is defined as the relative distance from  $(x, y)$  to the  $i$ th sensing path, which is expressed as

$$R_i(x, y) = \frac{D_{a,i}(x, y) + D_{s,i}(x, y)}{D_i} - 1 \quad (3)$$

where  $D_i$  is the distance between the actuator and the sensor for the  $i$ th sensing path, while  $D_{a,i}(x, y)$  and  $D_{s,i}(x, y)$  are, respectively, the distances between  $(x, y)$  and the actuator and the sensor for the  $i$ th sensing path, as shown in Figure 1.

It is assumed that  $W_i[R_i(x, y)]$  is the non-negative linearly decreasing weight distribution function of the  $i$ th sensing path,<sup>22</sup> with its contour in the shape of a set of ellipses as illustrated in Figure 2.  $\beta$  is a scaling parameter that controls the size of the effective elliptical distribution area. The weight distribution function can be written as

$$W_i[R_i(x, y)] = \begin{cases} 1 - \frac{R_i(x, y)}{\beta}, & R_i(x, y) < \beta \\ 0, & R_i(x, y) \geq \beta \end{cases} \quad (4)$$

### The dominance effect of the weight distribution

It has been shown that the damage localization result of the PDI algorithm is highly dependent on the weight distribution,<sup>19,21,23</sup> which is influenced by both the network of sensing paths and the value of  $\beta$  of individual sensing paths.

As in Wang et al.,<sup>24</sup> a concept of the unit weight distribution is proposed to estimate the elliptical distribution; it is defined as

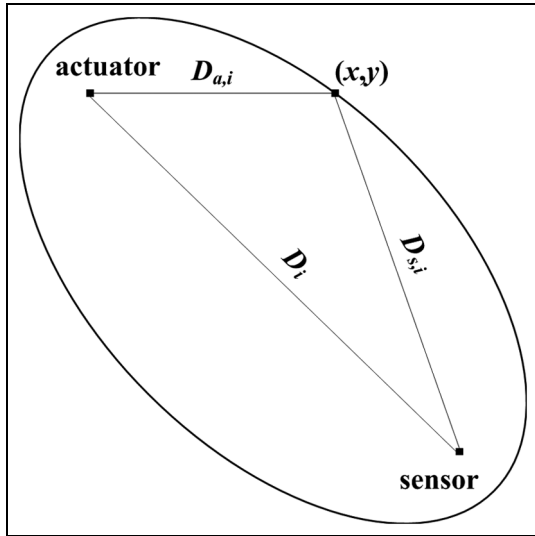


**Figure 1.** The illustration of relative distance  $R_i$ .

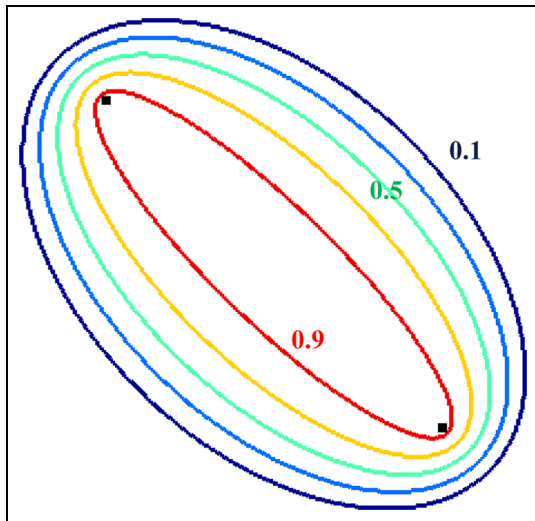


**Figure 2.** The contour illustration of weight distribution function  $W_i$ .

$$U(x,y) = \sum_{i=1}^N W_i[R_i(x,y)] \quad (5)$$

Here, the  $DI_i$  in equation (1) is assumed to be unit and the weight distributions of all paths are summed. This function considers both the network of sensing paths and the scaling parameter  $\beta$  simultaneously, and the higher the unit weight distribution density value, the higher chance that the signal change in the affected sensing path is mapped there. It has been demonstrated that the points with high unit weight distribution density value, which are usually on the intersections of the sensing paths, show a dominance of damage localization sensitivity.<sup>23</sup>

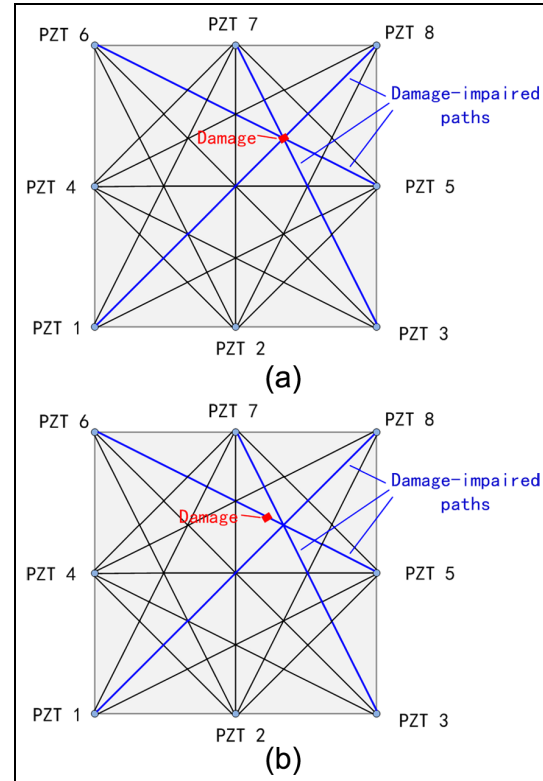


**Figure 3.** Typical cases of the PDI approach: (a) Case 1 and (b) Case 2.

Figure 3 shows the mechanism of how the weight distribution influences the accuracy of damage localization in the PDI algorithm. In a typical network of sensing paths<sup>22</sup> as illustrated in Figure 3, Case 1: when damage locates on the intersection of paths 3-7, 1-8, and 5-6, these paths would be seriously damage-impaired as shown in Figure 3(a). Then, the peak point of the probability image would be close to the actual damage while the high damage indices of the damage-impaired paths are mapped on the intersection. Therefore, the accuracy of damage localization would be very high. However, Case 2: when damage locates on path 5-6 with a little distance from the intersection as shown in Figure 3(b), the peak point of the probability image would be close to the intersection. Although the damage indices of path 3-7 and 1-8 are lower than that in Case 1, it will not change the location of the peak point of the probability image considerably since the high damage indices of the damage-impaired paths are also mapped on the intersection (the corresponding experimental results can be seen in Wang et al.<sup>22</sup>). Therefore, the accuracy of damage localization will suffer.

#### The WCPDI approach

Increasing the number of sensing paths is a common method to reduce the error of damage localization in

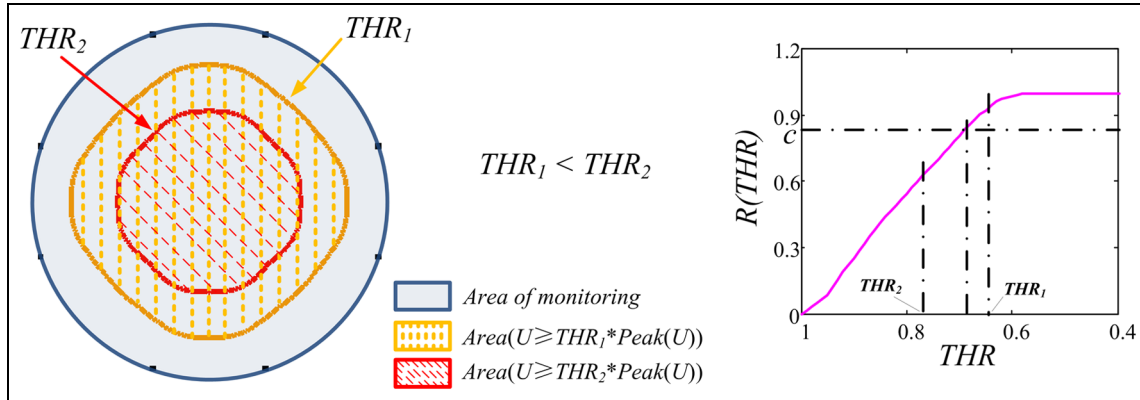


**Figure 4.** The illustration of the area above  $THR$  and the monitored area.

the PDI algorithm. However, it is uneconomical since the use of more paths increases the cost of monitoring. Since the points with high unit weight distribution density value show a dominance of damage localization sensitivity, it is feasible to inhibit the dominance effect by compensating the probability image  $P$  using the unit weight distribution  $U$ . Therefore, under the same sensor configuration, a WCPDI is introduced as

$$WCPDI(x, y) = \begin{cases} \frac{P(x, y) - THR \cdot \text{peak}(P)}{U(x, y) / \text{peak}(U)}, & \text{if } P(x, y) > THR \cdot \text{peak}(P) \\ 0, & \text{others} \end{cases} \quad (6)$$

where  $\text{peak}(P)$  is the peak value of  $P(x, y)$ . As the peak point of the PDI probability image is not far from the actual damage, it is not necessary to compute in the total monitoring area. Therefore, only the area  $P(x, y) > THR \cdot \text{peak}(P)$  consisting of grids with probability values for the presence of damage above the threshold ( $THR$ ) is used for compensation.

$THR$  is a parameter to control the size of the effective compensation area and the intensity of weight compensation. A small  $THR$  makes the size of effective compensation area larger and the intensity of weight compensation stronger; a large  $THR$  makes the size of effective compensation area smaller and the intensity of weight compensation weaker. Moreover, if  $THR$  is too low, the result of the points with small unit weight distribution density value would become too large since the weight compensation is too strong. Contrarily, if  $THR$  is too high, the weight compensation would be invalid since it is too weak. **Therefore, appropriate selection of the  $THR$  value is critical for the WCPDI approach. Damage localization would not be improved if the  $THR$  is set either too low or too high.**

Here, a normalized histogram is employed to pick the  $THR$ . The construction process of the normalized histogram is described in Wang et al.<sup>24</sup> In this study,

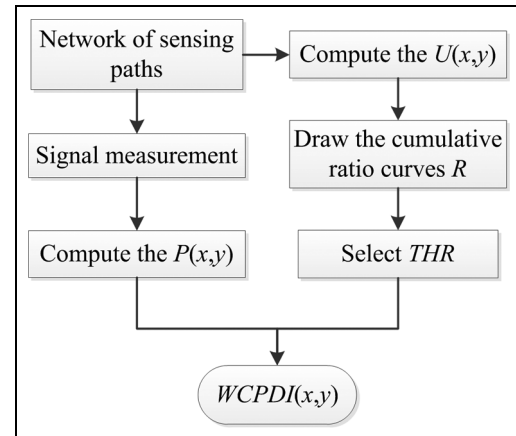


**Figure 5.** The WCPDI approach.

the histogram is used to roughly assess the probability distribution of a given  $U(x, y)$  from equation (5) by depicting the frequencies of observations occurring in certain ranges of values.<sup>23</sup> Then a suitable  $THR$  can be determined in terms of the cumulative ratio curve of the histogram, which is defined as

$$R(THR) = \frac{\text{Area}(U \geq THR \cdot \text{peak}(U))}{\text{Area of monitoring}} \quad (7)$$

where  $R(THR)$  is the ratio of the area above the  $THR$  to the area of monitoring, as shown in Figure 4. Only the points whose unit weight distribution density values are higher than  $THR$  are considered for effective compensation area. The selection of  $THR$  could be determined by  $c$ , which is a parameter for controlling the ratio of effective compensation area to the area of monitoring, according to the cumulative ratio curve as shown in Figure 4.

The general principle of the WCPDI approach is illustrated in Figure 5, and the key steps are described as follows:

**Table 1.** Characteristics of composite panel and PZT sensors.

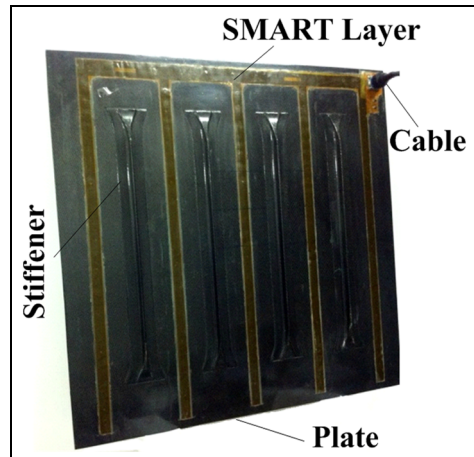
Composite panel	PZT sensors
Dimensions of panel	$710 \text{ mm} \times 734 \text{ mm} \times 4 \text{ mm}$
Stacking configuration	(+45°/0°/-45°/90°)2S
T-shaped stiffeners	507 mm × 4.9 mm × 15 mm
Voltage constant $e_{33}$ (Farad/m)	$15 \times 10^{-9}$
Charge constant $d_{31}$ (m/V)	$-168 \times 10^{-12}$
Relative dielectric constant $K^T$	1950

**Table 2.** Details of different groups of sensing paths.

Group	Sensors' number	Paths included	Direct distance (mm)	Monitoring area (mm <sup>2</sup> )
CIR	8	40	342–485	184,750
SQU	16	84	148–213	205,128

- After a sensor layout being defined and the operating paths being determined, the normalized unit weight distribution  $U(x, y)$  can be calculated using equation (5).
- Generate the cumulative ratio curves  $R(THR)$  using equation (7).
- Select the  $THR$  with condition  $R(THR) = c$ .
- Measure signals and compute the  $P(x, y)$  using equation (1).
- Calculate the  $WCPDI(x, y)$  using equation (6).

Through this WCPDI algorithm, damage localization can be realized with little influence by the dominance effect of the weight distribution, which means the localization accuracy will be improved compared to the localization result merely based on the peak point of the PDI probability image.

**Figure 6.** The stiffened composite panel.

## Specimen and experimental setup

### Stiffened composite panel

Figure 6 shows a U7192 carbon fiber composite panel with four T-shaped stiffeners that was acquired from the COMAC for this study, and a number of APC851 PZT sensors are mounted on the composite panel. The main characteristics of composite panel and PZT sensors are listed in Table 1. The dimensions of PZT sensors are 6.25 mm in diameter and 0.23 mm in thickness. The sampling rate for sensor data acquiring was set at 24 MHz. The Hann window-modulated five-peak sine burst exciting signal with 325 kHz was driven to the actuators in this specimen.

### Different configurations of sensing paths

As the unit weight distribution is highly dependent on the configuration of sensing paths, the developed

diagnostic imaging algorithm was validated with two different groups of sensing paths: CIR (enclose a circle monitoring area) and SQU (enclose a square monitoring area) in this study. The sensors' number, paths' number, direct distance, and monitoring area of each group are summarized in Table 2, and two configurations are illustrated in Figure 7. In general, the stiffeners affect the wave propagation properties; however, these influences can be removed by the subtraction between baseline and the current signal in the same environment. Therefore, the stiffened plates had often been chosen for the PDI research, for example, the wing skin with L-shaped stiffeners in Zhao et al.<sup>19</sup> and the composite panel with multiple T-shaped stiffeners in Wang et al.<sup>21</sup> The area with stiffeners is generally avoided in the selection of sensor position to guarantee the performance and activity of the sensors. Therefore, the PZT sensors are mounted in parallel lines between the stiffeners in this study.

Here, the square sensor configuration is less efficient than the circular for the PDI algorithm as indicated in Wu et al.<sup>23</sup> However, in this article, it is not our objective to compare the detectability of different sensor configurations, but just verify the performance of the WCPDI algorithm in various sensing configurations.

The unit weight distribution (from equation (5)) is shown in Figure 8, which is dependent on the given

configuration of sensing paths and the scaling parameter  $\beta$  of individual sensing paths. The small white squares indicate the location of PZT sensors. The high unit weight distribution density value indicates the high chance that the signal change in damage-impaired sensing path is mapped there while these points are often affected by a large number of damage-impaired sensing paths. Therefore, the diagnostic results are made sensitive not only to defect but also to the number of potential damage-impaired sensing paths.

The corresponding cumulative ratio curves (from equation (7)) for different configurations with different values of  $\beta$  are shown in Figure 9. The parameters of *THR* could be determined by  $c$  according to the cumulative ratio curves for different  $\beta$  as shown in Figure 9.

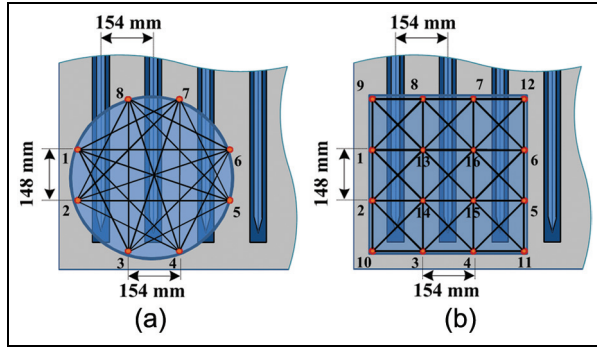


**Figure 7.** Diagram of different configurations of sensing paths, where the small circles indicate sensor locations and the large shaded circle and rectangle are the monitoring areas: (a) Group CIR and (b) Group SQU.

## Results and discussion

### Damage localization

Then, the experimental results are assessed to validate the feasibility of applying the proposed technique for damage localization. To reduce experiment cost,<sup>4,26</sup> 11 artificial damage cases of different positions with a kind of solid adhesive tape of size  $12 \times 12 \times 3 \text{ mm}^3$ , respectively, bonded on the surface of the panel in this study.

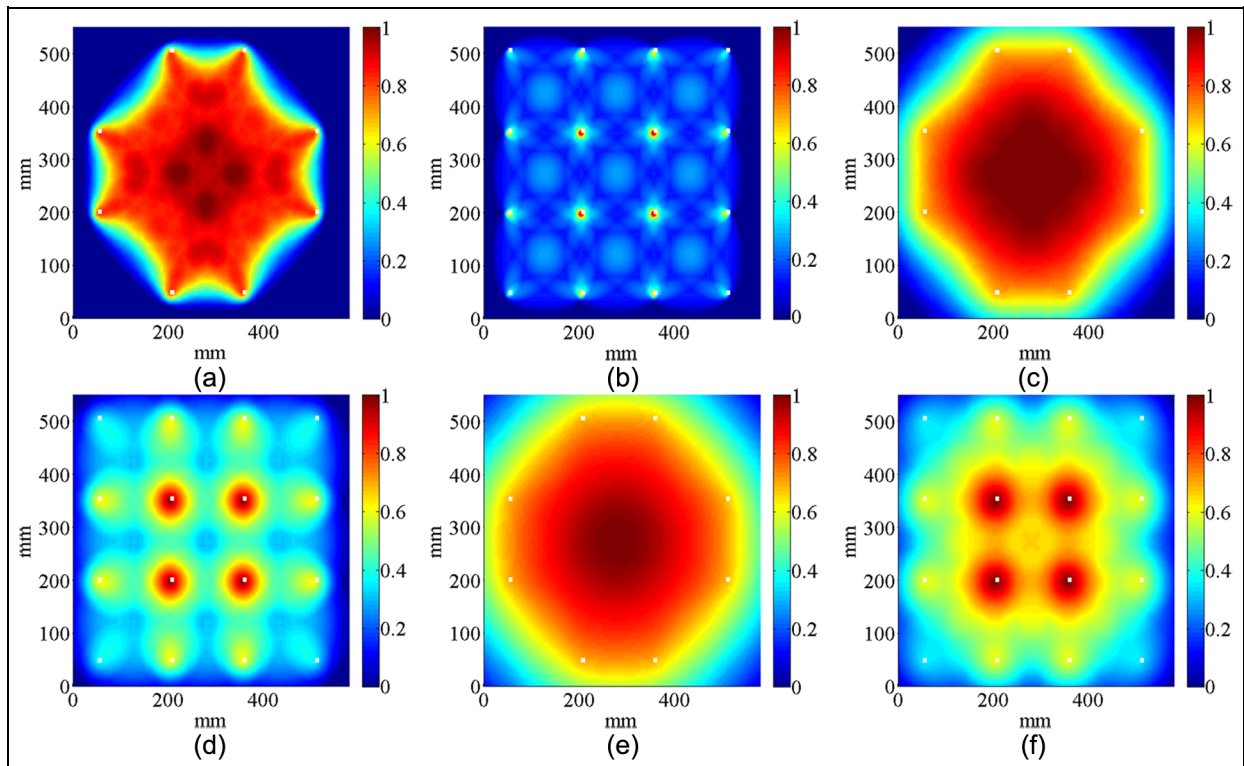


**Figure 8.** Normalization maps of unit weight distribution for different groups and different  $\beta$ : (a) Group CIR,  $\beta = 0.1$ ; (b) Group SQU,  $\beta = 0.1$ ; (c) Group CIR,  $\beta = 0.5$ ; (d) Group SQU,  $\beta = 0.5$ ; (e) Group CIR,  $\beta = 0.9$ ; and (f) Group SQU,  $\beta = 0.9$ .

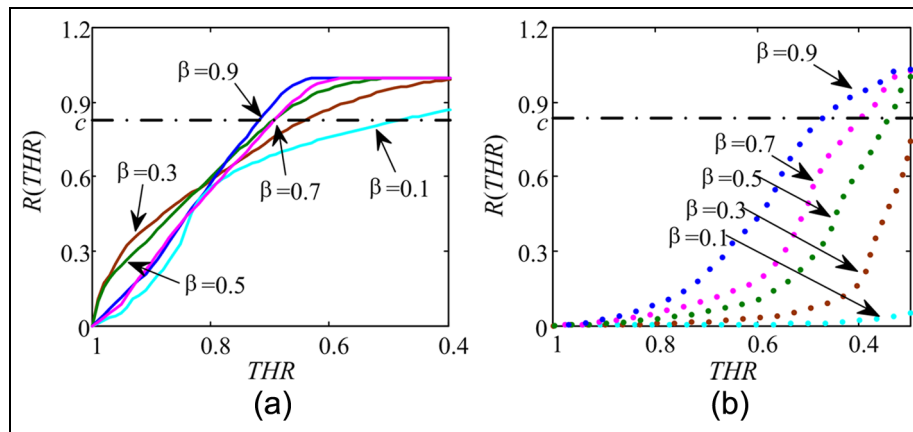


**Figure 9.** The cumulative ratio curves for different  $\beta$ : (a) Group CIR and (b) Group SQU.

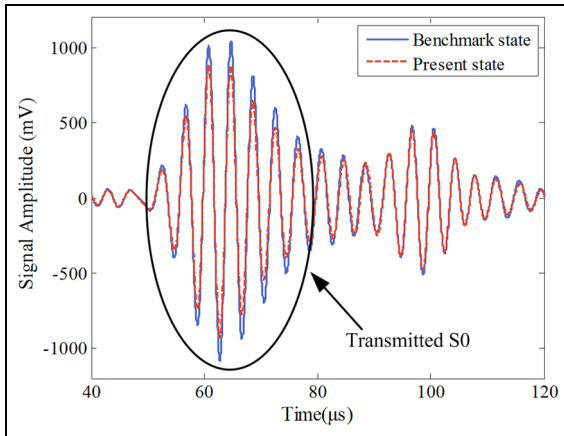


**Figure 10.** Sample waveforms of the sensor path 8-16.

Guided wave signals were captured experimentally in both the benchmark and present states (before and after the artificial damage was introduced). The WCPDI is based on comparing the current sensor responses to the previously recorded benchmark sensor responses. However, it is known that environmental effects, such as temperature differences, will also cause changes in the sensor signals and will thus interfere with most damage detection schemes. Therefore, a calibration technique utilizing multiple benchmarks that has been proposed by Beard et al.<sup>27</sup> is employed to mitigate the effects of environmental changes.

The signals from path 8-16 at 325 kHz are displayed in Figure 10. The blue solid lines represent the signals in the benchmark state, while the red dashed lines represent the signals in the present state. The first arrival wave packet, which is associated with the transmitted fundamental symmetric S0 mode, is selected for computing the correlation coefficient in this study.

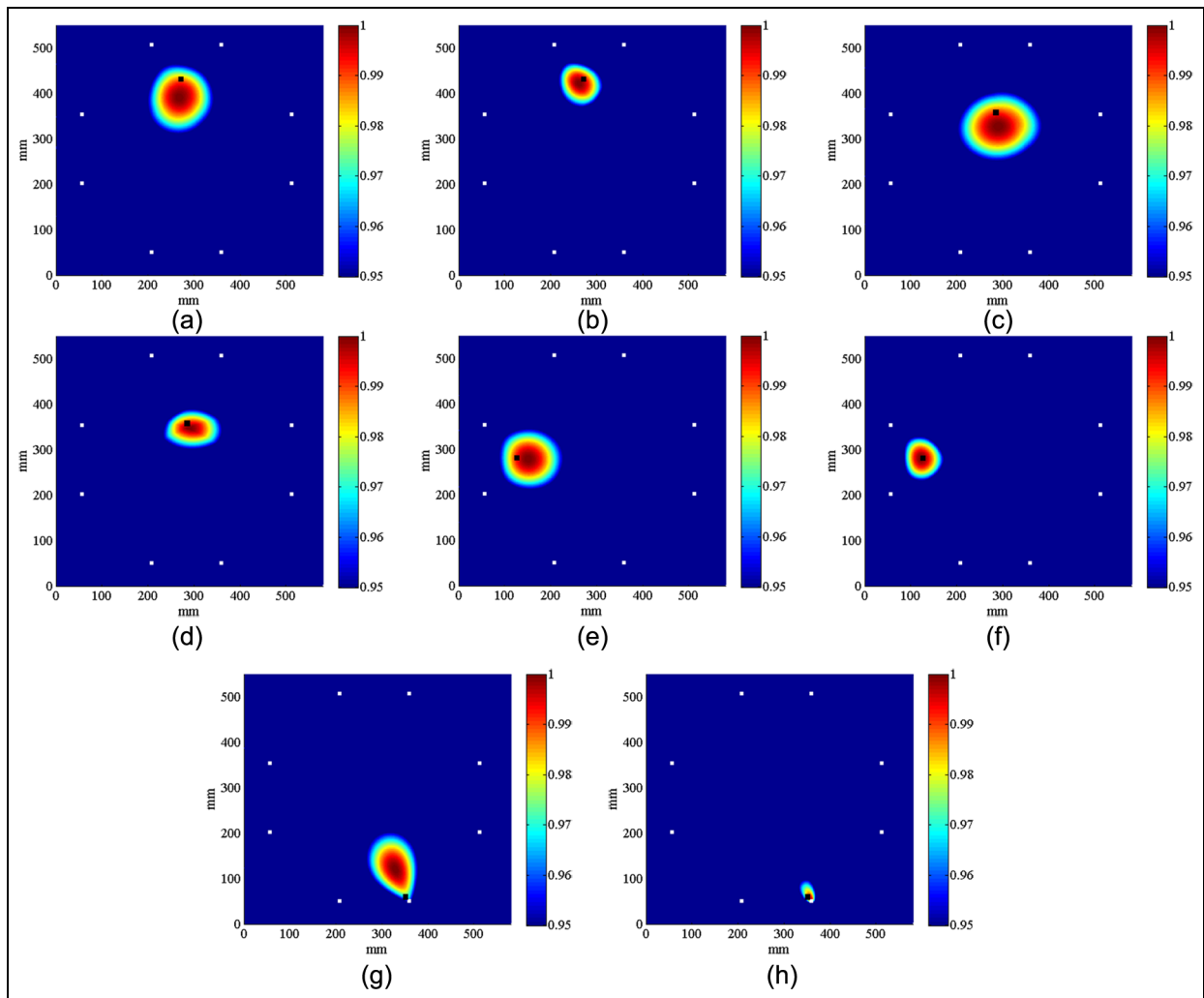
Two initial settings are made as follows: the scaling parameter  $\beta=0.7$  and the ratio  $c=0.9$ .

Figure 11(a), (c), and (e) shows the probability images (from equation (1)) from Group CIR at 325 kHz with 95% image threshold. The small white squares indicate the location of PZT sensors and the large black one indicates the artificial damage. Obviously, the dominance of high unit weight distribution density value has a prominent influence on the localization result of the PDI algorithm, while the diagnostic damage locations are tending to the center of the monitoring area which is the peak of unit weight distribution as shown in Figure 11(e).

Conversely, the WCPDI algorithm (from equation (6)) shows a good performance for damage localization as shown in the right side of Figure 11. Besides Group CIR, Group SQU also shows the better performance of the WCPDI algorithm as shown in Figure 12.

Tables 3 and 4 list the damage monitoring results of Group CIR and Group SQU, respectively, among which damage localizations are given based on the peak points of the probability images. The errors in tables are the distance between the peak points of the individual images and actual locations of damages.

The WCPDI has increased the localization error over conventional PDI in several cases where the damage is located on the interactions of several sensing paths, for example, D02 and D07 from Group CIR in Table 3 and D05 from Group SQU in Table 4. In these cases, the peak point of the probability image would be close to the actual damage while the high damage indices of the damage-impaired paths are mapped on the intersections. Therefore, the accuracy of damage localization in these cases is very high for the conventional PDI. However, the WCPDI algorithm has changed the location of the peak point since the probability image is compensated with the unit weight of various positions to inhibit the path weight difference effect. Therefore, the localization error in these cases has been increased in the WCPDI.



**Figure 11.** Diagnostic images of PDI algorithm and WCPDI from Group CIR with  $c = 0.9$  and  $\beta = 0.7$ : (a) PDI, (b) WCPDI, (c) PDI, (d) WCPDI, (e) PDI, (f) WCPDI, (g) PDI, and (h) WCPDI.

**Table 3.** Damage localization results of Group CIR (units: mm).

	Actual damages	PDI localization	Error	WCPDI localization	Error
D01	(272,431)	(269,387)	44.10	(266,425)	8.49
<b>D02</b>	<b>(287,283)</b>	<b>(291,289)</b>	<b>7.21</b>	<b>(284,302)</b>	<b>19.24</b>
D03	(285,357)	(281,315)	42.19	(283,350)	7.28
D04	(357,287)	(329,281)	28.64	(361,295)	8.94
D05	(127,281)	(151,279)	24.08	(123,280)	4.12
D06	(131,353)	(170,334)	43.38	(117,346)	15.65
<b>D07</b>	<b>(351,349)</b>	<b>(347,351)</b>	<b>4.47</b>	<b>(367,372)</b>	<b>28.02</b>
D08	(351, 59)	(328,121)	66.13	(355, 64)	6.40
D09	(275,289)	(275,211)	22.00	(267,188)	8.06
D10	(213,295)	(223,306)	15.16	(203,310)	18.03
D11	(299,375)	(303,358)	17.46	(301,378)	3.61
Average			28.62		11.62

PDI: probability-based diagnostic imaging; WCPDI: weight-compensated probability-based diagnostic imaging.

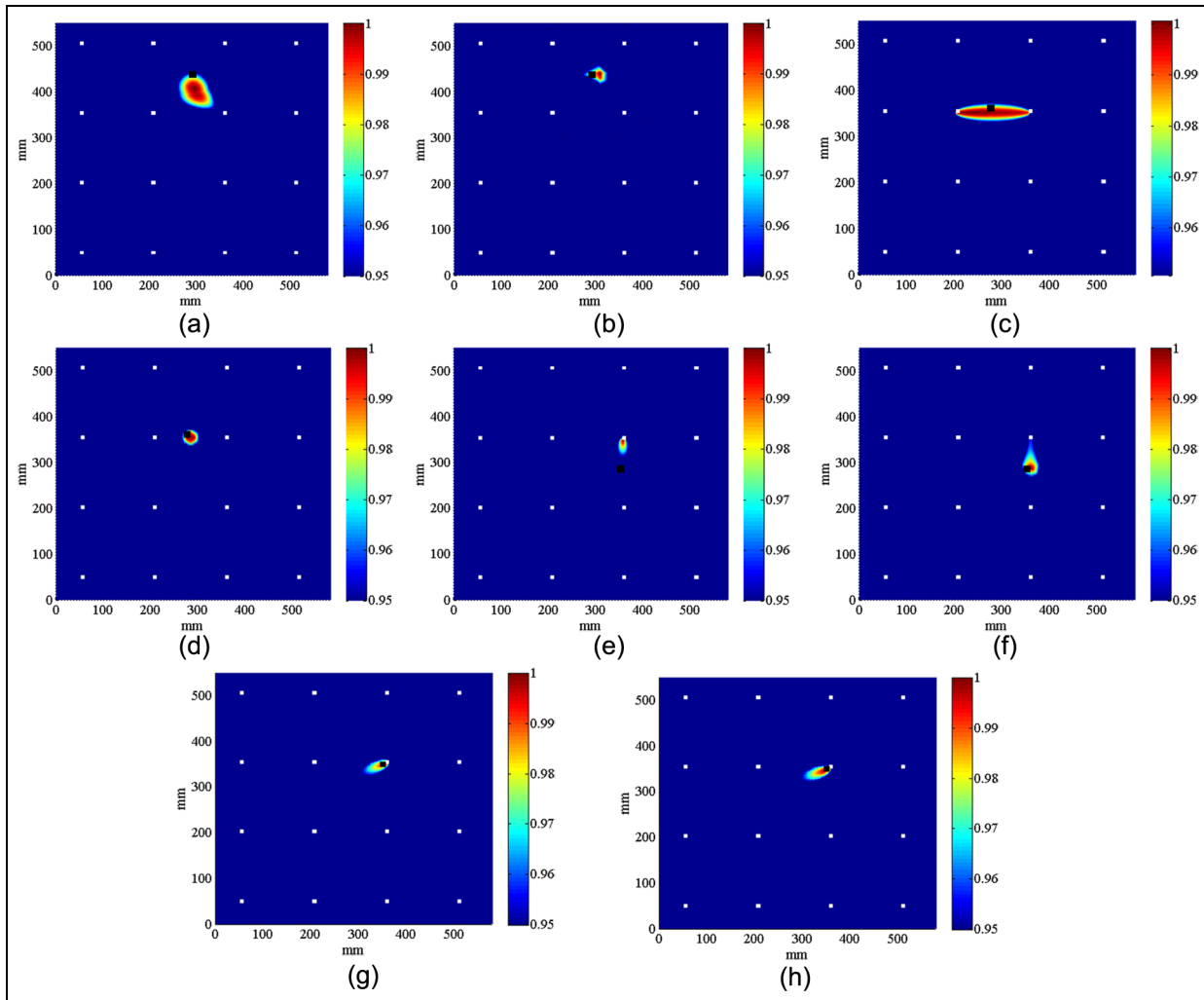


**Figure 12.** Diagnostic images of PDI algorithm and WCPDI from Group SQU with  $c = 0.9$  and  $\beta = 0.7$ : (a) PDI, (b) WCPDI, (c) PDI, (d) WCPDI, (e) PDI, (f) WCPDI, (g) PDI, and (h) WCPDI.

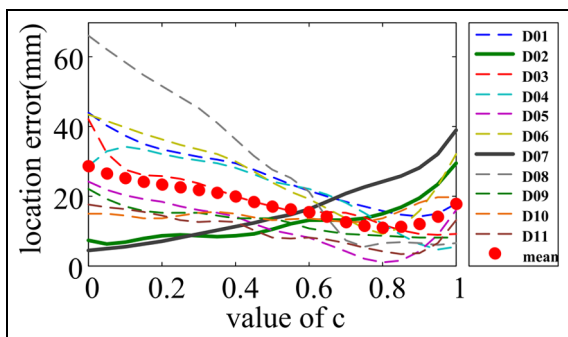


**Figure 13.** The localization errors with different values of  $c$  in D01-D11 cases from Group CIR.

Contrarily, the WCPDI algorithm has decreased localization error over conventional PDI in the other cases. As most of the areas are not on the interactions,

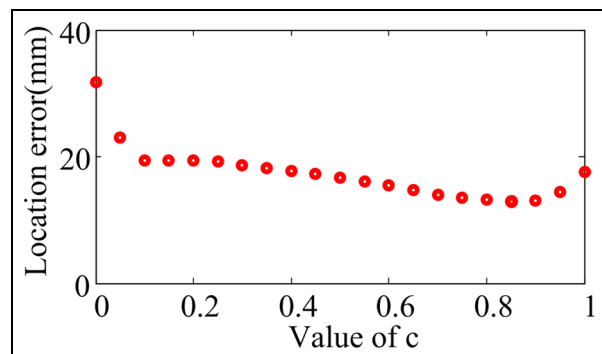


**Figure 14.** Averaged localization error with different values of  $c$  (both Group CIR and SQU).

the average error would be decreased by using the WCPDI algorithm. From Group CIR, the PDI algorithm localizes damages with an average localization

**Table 4.** Damage localization results of Group SQU (units: mm).

	Actual damages	PDI localization	Error	WCPDI localization	Error
D01	(272,431)	(295,407)	33.24	(309,441)	38.33
D02	(287,283)	(293,237)	46.39	(285,250)	33.06
D03	(285,357)	(210,354)	75.06	(277,356)	8.06
D04	(357,287)	(360,353)	66.07	(359,286)	2.24
D05	(127,281)	(132,278)	5.83	(103,280)	24.02
D06	(131,353)	(155,353)	24.00	(123,354)	8.06
D07	(351,349)	(357,354)	7.81	(351,347)	2.00
D08	(351,59)	(359,51)	11.31	(359,50)	12.04
D09	(275,189)	(248,193)	27.29	(283,188)	8.06
D10	(213,295)	(208,352)	57.22	(207,286)	10.82
D11	(299,375)	(329,367)	31.05	(289,384)	13.45
Average			35.03		14.56

PDI: probability-based diagnostic imaging; WCPDI: weight-compensated probability-based diagnostic imaging.

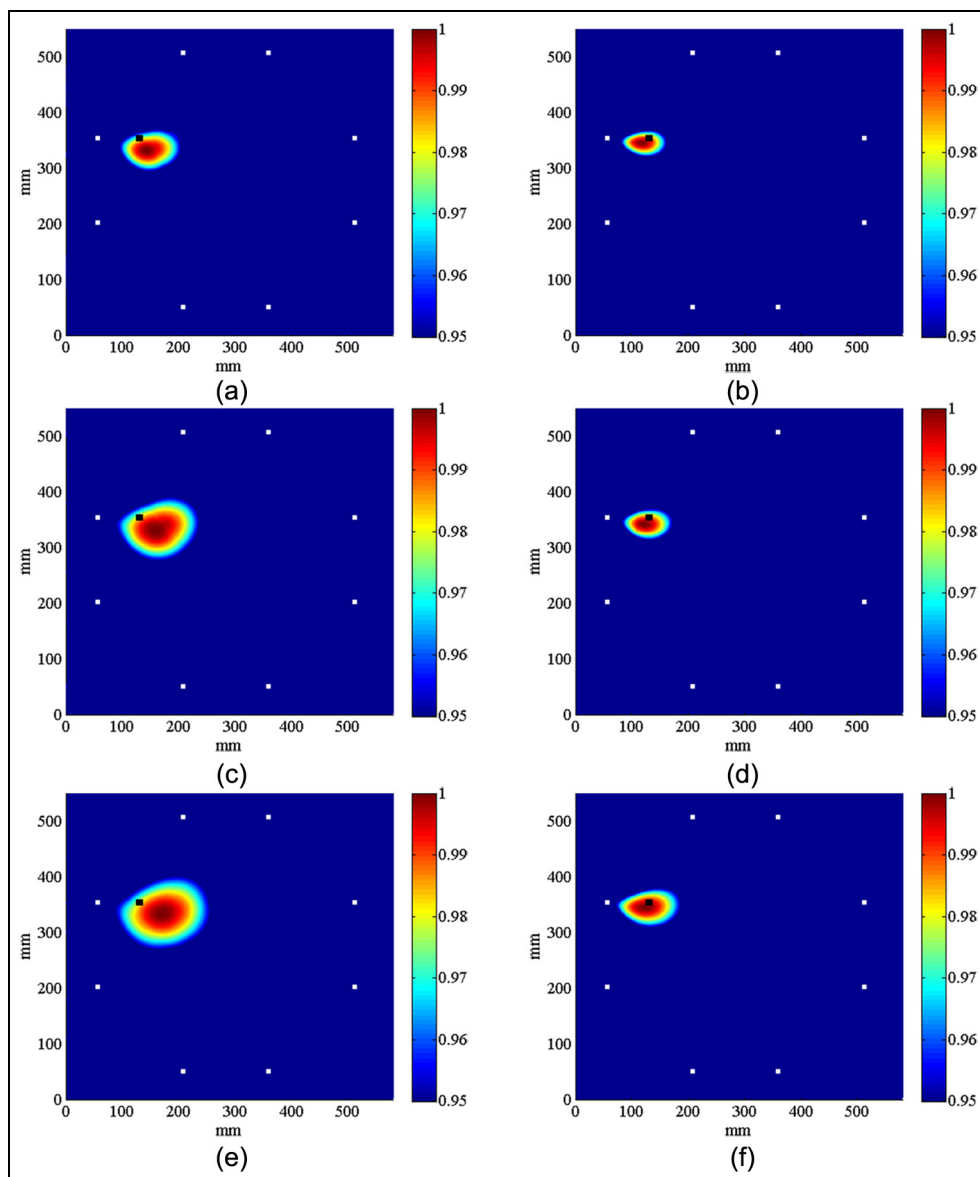


**Figure 15.** Diagnostic images of PDI algorithm (left side) and WCPDI (right side) from Group CIR with different  $\beta$ : (a) PDI,  $\beta = 0.3$ ; (b) WCPDI,  $\beta = 0.3$ ; (c) PDI,  $\beta = 0.5$ ; (d) WCPDI,  $\beta = 0.5$ ; (e) PDI,  $\beta = 0.7$ ; and (f) WCPDI,  $\beta = 0.7$ .

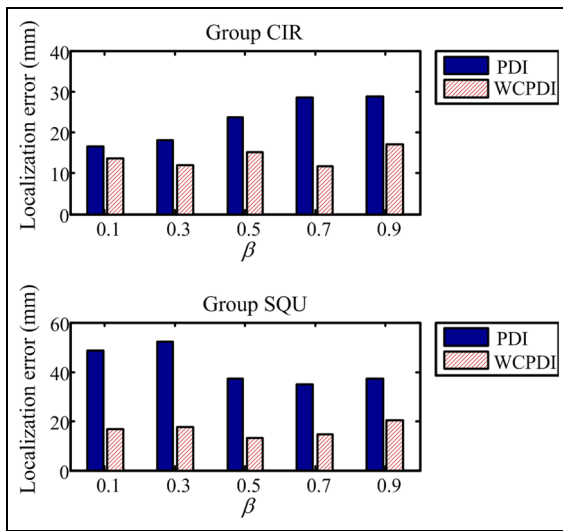


**Figure 16.** Averaged localization errors of the PDI algorithm and the WCPDI algorithm with different  $\beta$ .

error of 28.62 mm, while the WCPDI algorithm realizes with an average localization error of 11.62 mm. Similarly, the average error of Group SQU is decreased from 35.03 to 14.56 mm by using the WCPDI algorithm. As the dominance of high unit weight distribution density value is available inhibited, the developed algorithm could obtain more accurate localization than the conventional one.

### Parameter study

The parameter  $c$  is first discussed. Figure 13 shows the localization errors of D01–D11 cases from Group CIR when  $c$  ranges from 0 to 1.0 with an interval of 0.05. The averaged localization error with different values of  $c$  is presented as the “mean” red points. D02 and D07 cases in which the PDI algorithm ( $c = 0$ ) performed well are depicted with bold curves in Figure 13 while the localization error increased with  $c$ . When the PDI algorithm ( $c = 0$ ) performed worse in the other cases, the localization error decreased with  $c$ . Therefore, if a new sensor arrangement with more sensing paths is employed, the  $c$  should be smaller since the PDI algorithm could perform well; if a sparse sensor arrangement with a little sensing paths is employed, the  $c$  should be bigger since the PDI algorithm could not perform poorly.

Figure 14 shows the average localization error of all 11 damages when  $c$  ranges from 0 to 1.0 with an interval of 0.05. It is observed that when  $c$  equals 0.85, the averaged localization error reaches the minimum value of 13 mm, while it reaches the maximum of 31 when  $c$  equals 0, which is the localization result merely based on the PDI algorithm. In the following discussion,  $c$  is set as 0.85.

The effect of  $\beta$  on identifying the damage using the WCPDI algorithm is also investigated in this study. As different  $THR$  would be selected while the unit weight distribution  $U(x, y)$  is changed with  $\beta$ , the WCPDI algorithm would have a good performance in different  $\beta$  as shown in Figure 15. Figure 16 shows the average localization error of all 11 damages when  $\beta$  ranges from 0.1 to 0.9 with an interval of 0.2. It is observed that the developed algorithm obtains more accurate localization than the conventional one in different  $\beta$ . To further limit the effect of arbitrary choices of  $\beta$  on the identification accuracy, a fusion technique that has been proposed by Wang et al.<sup>24</sup> could be used.

### Conclusion

This study extended the previous work of probabilistic diagnostic imaging approach and developed a weight compensated-based damage probabilistic diagnostic imaging algorithm to improve the ability of damage localization with higher precision under the same sensor configuration. The process of how to realize the WCPDI algorithm was presented. The effectiveness of the algorithm was thoroughly assessed over several simulated defect locations. The proposed algorithm showed great potential for defect localization for SHM of aircraft structures. More tests on multi-defects may be needed to further prove the effectiveness of the proposed approach, because multi-damage causes much more complex scattering phenomena in captured signals than mono-damage does.

### Acknowledgements

The authors are grateful for the support of Beijing Aeronautical Science and Technology Research Institute of COMAC in providing the test specimen.

### Declaration of Conflicting Interests

The author(s) declared no potential conflicts of interest with respect to the research, authorship, and/or publication of this article.

### Funding

The author(s) disclosed receipt of the following financial support for the research, authorship, and/or publication of this article: This research was supported by the National Natural Science Foundation of China (grants nos 11172053, 91016024, 51475067). The authors also thank the support of the Fundamental Research Funds for the Central Universities (NCET-11-0055).

### References

- Chang FK, Markmiller JF, Yang J, et al. Structural health monitoring. In: Johnson SB, Gormley T,

- Kessler S, et al. (eds) *System health management: with aerospace applications*. Chichester: John Wiley & Sons, Ltd, 2011, pp. 419–428.
2. Boller C, Chang FK and Fujino Y. *Encyclopedia of structural health monitoring*. Chichester: John Wiley & Sons, Ltd, 2009.
  3. Wu ZJ, Qing XP, Ghosh K, et al. Health monitoring of bonded composite repair in bridge rehabilitation. *Smart Mater Struct* 2008; 17: 45–59.
  4. Sohn H, Park G, Wait JR, et al. Wavelet-based active sensing for delamination detection in composite structures. *Smart Mater Struct* 2004; 13: 153–160.
  5. Diligent O, Lowe MJS and Cawley P. Reflection and scattering of the S-0 Lamb mode from 3-D circular defects in plates. In: Thompson DO and Chimenti DE (eds) *Review of progress in quantitative nondestructive evaluation*, vol. 615, Brunswick, Maine, 29 July–3 August 2001, pp. 231–238.
  6. Hong M, Su Z, Wang Q, et al. Modeling nonlinearities of ultrasonic waves for fatigue damage characterization: theory, simulation, and experimental validation. *Ultrasonics* 2014; 54: 770–778.
  7. Demma A, Cawley P and Lowe M. Scattering of the fundamental shear horizontal mode from steps and notches in plates. *J Acoust Soc Am* 2003; 113: 1880–1891.
  8. Su Z and Ye L. *Identification of damage using Lamb waves: from fundamentals to applications*. London: Springer, 2009.
  9. Qing XLP, Beard SJ, Kumar A, et al. Advances in the development of built-in diagnostic system for filament wound composite structures. *Compos Sci Technol* 2006; 66: 1694–1702.
  10. Michaels JE. Detection, localization and characterization of damage in plates with an in situ array of spatially distributed ultrasonic sensors. *Smart Mater Struct* 2008; 17: 03503501–03503515.
  11. Ye L, Lin Y, Dong W, et al. Damage detection in a large composite panel of five stiffeners using Lamb wave signals. *Mater Forum* 2009; 33: 136–142.
  12. Yu L and Giurgiutiu V. In-situ optimized PWAS phased arrays for Lamb wave structural health monitoring. *J Mech Mater Struct* 2007; 2: 459–487.
  13. Prasad SM, Balasubramaniam K and Krishnamurthy CV. Structural health monitoring of composite structures using Lamb wave tomography. *Smart Mater Struct* 2004; 13: 73–79.
  14. Breon LJ, Van Velsor JK and Rose JL. Guided wave damage detection tomography for structural health monitoring in critical zones of pipelines. *Mater Eval* 2007; 65: 1215–1219.
  15. Wang CH, Rose JT and Chang FK. A synthetic time-reversal imaging method for structural health monitoring. *Smart Mater Struct* 2004; 13: 415–423.
  16. Ihn JB and Chang FK. Pitch-catch active sensing methods in structural health monitoring for aircraft structures. *Struct Health Monit* 2008; 7: 5–19.
  17. Cai J, Shi LH, Yuan SF, et al. High spatial resolution imaging for structural health monitoring based on virtual time reversal. *Smart Mater Struct* 2011; 20: 1–11.
  18. Zhou C, Su Z and Cheng L. Probability-based diagnostic imaging using hybrid features extracted from ultrasonic Lamb wave signals. *Smart Mater Struct* 2011; 20: 12500501–12500514.
  19. Zhao X, Gao H, Zhang G, et al. Active health monitoring of an aircraft wing with embedded piezoelectric sensor/actuator network: I—defect detection, localization and growth monitoring. *Smart Mater Struct* 2007; 16: 1208–1217.
  20. Koduru JP and Rose JL. Guided wave annular array sensor design for improved tomographic imaging. In: Thompson DO and Chimenti DE (eds) *Review of progress in quantitative nondestructive evaluation*, vol. 28. Chicago, IL: AIP Publishing, 2009, pp. 658–665.
  21. Wang D, Ye L, Lu Y, et al. Probability of the presence of damage estimated from an active sensor network in a composite panel of multiple stiffeners. *Compos Sci Technol* 2009; 69: 2054–2063.
  22. Wang D, Ye L, Su ZQ, et al. Probabilistic damage identification based on correlation analysis using guided wave signals in aluminum plates. *Struct Health Monit* 2010; 9: 133–144.
  23. Wu Z, Liu K, Wang Y, et al. Validation and evaluation of damage identification using probability-based diagnostic imaging on a stiffened composite panel. *J Intel Mat Syst Str* 2014; 26: 2181–2195.
  24. Wang D, Ye L, Lu Y, et al. A damage diagnostic imaging algorithm based on the quantitative comparison of Lamb wave signals. *Smart Mater Struct* 2010; 19: 065008.
  25. Ihn JB and Chang FK. Detection and monitoring of hidden fatigue crack growth using a built-in piezoelectric sensor/actuator network: I—diagnostics. *Smart Mater Struct* 2004; 13: 609–620.
  26. Qiu L, Liu ML, Qing XL, et al. A quantitative multidamage monitoring method for large-scale complex composite. *Struct Health Monit* 2013; 12: 183–196.
  27. Beard S, Liu C-C and Chang F-K. Design of a robust SHM system for composite structures. In: *Industrial and commercial applications of smart structures technologies 2007*, San Diego, CA, 19–20 March 2007, p. 652709. Bellingham, WA: SPIE.